



# Investigation of Structural, Morphological and Elastic Properties of Ni-Zn Ferrite Grown with an Oxalate Precursor

N. D. Chaudhari<sup>1</sup> · D. Y. Nadargi<sup>2</sup> · S. M. Kabbur<sup>3</sup> · R. C. Kambale<sup>4</sup> · A. Das<sup>5</sup> · S. S. Suryavanshi<sup>2</sup>

Received: 24 November 2021 / Accepted: 9 March 2022 / Published online: 30 March 2022  
© The Minerals, Metals & Materials Society 2022

## Abstract

We report structural, morphological and elastic properties of  $\text{Ni}_x\text{Zn}_{1-x}\text{Fe}_2\text{O}_4$  ( $x = 0.28, 0.30, 0.32, 0.34, 0.36, 0.38, 0.40$ ) ferrimagnetic oxides prepared using oxalate chemistry. The Rietveld refinement of the X-ray diffraction patterns confirm the formation of spinel cubic structure. The experimental and theoretical lattice constant is found to decrease with increasing  $\text{Ni}^{2+}$  content. The FTIR spectra exhibit two main fundamental absorption bands, one for the tetrahedral site around  $575$  to  $580\text{ cm}^{-1}$  and the other for the octahedral site around  $411$ – $413\text{ cm}^{-1}$ . The magnitude of elastic moduli is found to be independent with increasing  $\text{Ni}^{2+}$  content. The morphological analysis showed the formation of small and homogeneous particles, which is possible using an oxalate precursor. The elemental analysis confirmed the presence of Ni, Zn, Fe, and O as per their stoichiometric amounts. The structural, morphological and elastic properties are described with an interplay of oxalate precursor synthesis route of the ferrite development.

**Keywords** Ni-Zn ferrites · oxalate precursors · X-ray diffraction · FTIR · elastic constants

## Introduction

In recent years, spinel ferrites have attracted wide attention due to their diverse fields of application such as CO hydrogenation, optoelectronic devices, biomedical, and wastewater treatment.<sup>1–4</sup> Especially for high-frequency applications, spinel ferrites are the potential candidates due to their chemical and mechanical robustness, high resistivity, moderate

saturation magnetization, moderate permeability, high Curie temperature, and low power losses at high frequency.<sup>5</sup> Amongst the various ferrites, nickel ferrite ( $\text{NiFe}_2\text{O}_4$ ) is a versatile oxide with an inverse spinel structure that has low eddy currents losses, high electrical resistivity, high  $\mu_r$ , and high Ms. They are almost complimentary for applications such as multilayer chip inductor (MLCI) components and surface mount devices (SMD).<sup>6</sup> Similarly, zinc ferrite ( $\text{ZnFe}_2\text{O}_4$ ) also has a diverse array of applications such as gas sensors, photocatalyst, casting, and bio-products.<sup>7–9</sup> The combination of these two ferrites ( $\text{Ni}_x\text{Zn}_{1-x}\text{Fe}_2\text{O}_4$ ) is a mixed spinel ferrite and has fascinating magnetic properties such as high saturation magnetization, high initial permeability, and high Curie temperature, along with high resistivity and low power losses at high frequency. The general formula of spinel lattice is  $\text{AB}_2\text{O}_4$  in which  $\text{Zn}^{2+}$  ions are located on the tetrahedral A site,  $\text{Ni}^{2+}$  ions on octahedral B site and  $\text{Fe}^{3+}$  ions involve both tetrahedral and octahedral sites. The distribution of different cations over tetrahedral and octahedral sites mainly depends on preparation methods, parameters and approaches.<sup>5</sup> The proper choice of cations and their distribution among the tetrahedral and octahedral sites of spinel lattice determines the electric and magnetic properties of ferrites. The ferrites are commonly synthesized

✉ D. Y. Nadargi  
digambar\_nadargi@yahoo.co.in

✉ S. S. Suryavanshi  
ssuryavanshi@rediffmail.com

<sup>1</sup> Department of Physics, Pratishthan Mahavidyalaya, Paithan, Aurangabad 431107, India

<sup>2</sup> School of Physical Sciences, PAH Solapur University, Solapur 413255, India

<sup>3</sup> Department of Physics, Shri Shivaji Mahavidyalaya, Barshi 413411, India

<sup>4</sup> Department of Physics, Savitribai Phule Pune University, Pune 411007, India

<sup>5</sup> Solid State Physics Division, Bhabha Atomic Research Centre, Mumbai 400085, India

by conventional solid-state reactions using well-mixed powders of component oxides and other salts to increase the reactivity of the component oxides. The conventional ceramic method for the preparation of high-performance ferrites, though successful for large-scale production, has several limitations such as a long heating times, high sintering temperature, loss of fine particle nature, and poor control of particle size.<sup>6,7</sup> In the state-of-the-art, to overcome these limitations, different soft chemistry approaches such as coprecipitation, sol-gel method, hydrothermal method, combustion method, microemulsion, and oxalate precursors are employed.<sup>10–13</sup> These synthesis routes of developing ferrite materials have greater control over stoichiometry, homogeneity, and phase purity at a relatively lower temperature.<sup>14–18</sup> Amongst the aforementioned routes, a robust synthesis approach to develop the complex spinel ferrites is the oxalate precursor method and is preferred due to its low decomposition temperature, nanomaterial yield, and inherent simplicity.<sup>19</sup> The route utilizes simple metal acetates and oxalate precursors in an aqueous solution, thus eliminating the need for organometallic precursors.

In the present work, we demonstrate an oxalate precursor route for developing nanocrystalline Ni-Zn ferrite with the general formula  $\text{Ni}_x\text{Zn}_{1-x}\text{Fe}_2\text{O}_4$  ( $x = 0.28, 0.30, 0.32, 0.34, 0.36, 0.38$  and  $0.40$ ) and study structural, morphological and elastic properties.

## Experimental Details

$\text{Ni}_x\text{Zn}_{1-x}\text{Fe}_2\text{O}_4$  ( $x = 0.28, 0.30, 0.32, 0.34, 0.36, 0.38$  and  $0.40$ ) was synthesized in two different steps: i) preparation of  $\text{Fe}^{2+}$  acetate and ii) ferrite precipitation using oxalate chemistry. The chemicals used in a typical synthesis were acetic acid ( $\text{CH}_3\text{COOH}$ ), nickel acetate ( $\text{Ni}(\text{CH}_3\text{CO}_2)_2 \cdot 4\text{H}_2\text{O}$ ), zinc acetate ( $\text{Zn}(\text{O}_2\text{CCH}_3)_2 \cdot 2\text{H}_2\text{O}$ ), iron metal powder ( $< 10 \mu\text{m}$ ) and ammonium oxalate monohydrate ( $(\text{NH}_4)_2\text{C}_2\text{O}_4 \cdot \text{H}_2\text{O}$ ). All reactants were reagent-grade quality obtained from Sigma Aldrich and were used as received.

Initially, ferrous acetate (II) was prepared by adding acetic acid and distilled water to the required amount of iron metal powder with continuous heating until the iron metal powder was completely dissolved. To avoid the oxidation of Fe(II) to Fe(III), the whole reaction was carried out in a  $\text{CO}_2$  atmosphere. In the stoichiometric balance, the required amounts of Ni-acetate and Zn-acetate solutions were prepared separately. All three acetates were filled into individual burettes (with stopper) and adjusted to the stand in such a way that acetates were added dropwise into a beaker containing warm ammonium oxalate solution. The reaction mixture was maintained at  $60^\circ\text{C}$  with constant stirring until the acetates were consumed completely. This ultimately yielded complex oxalate precipitate, which was

then filtered, washed and dried at room temperature. The as-prepared samples were calcined at  $350^\circ\text{C}$  for 3 h to get ferrite compositions as  $\text{Ni}_x\text{Zn}_{1-x}\text{Fe}_2\text{O}_4$  ( $x = 0.28, 0.30, 0.32, 0.34, 0.36, 0.38$  and  $0.40$ ). Final sintering was carried out in an air atmosphere at  $1000^\circ\text{C}$  for 4 h and naturally cooled down to room temperature (Scheme 1, See supplementary Fig. S1). The detailed discussion on material characterization techniques is made in the supplementary section (see supplementary data file), which highlights the new results in the present communication.

## Results and Discussion

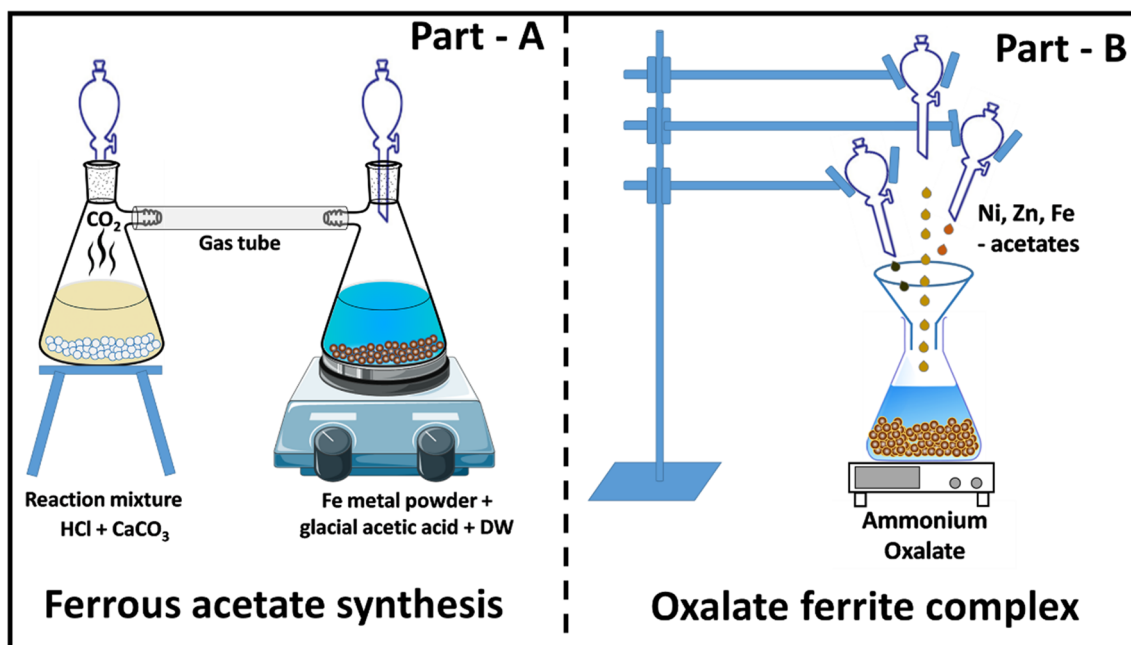
### Phase Identification Using XRD and Rietveld Analyses

The crystal structure of developed ferrite samples was confirmed by grazing incidence x-ray diffraction (XRD). Figure S2 (see supplementary Fig. S2) and Fig. 1 show XRD patterns of the calcined ( $350^\circ\text{C}$ , 3 h) and sintered ( $1000^\circ\text{C}$ , 4 h)  $\text{Ni}_x\text{Zn}_{1-x}\text{Fe}_2\text{O}_4$  ferrite system, respectively. Both the materials show the characteristic reflections of cubic spinel ferrites with the most intense [311] reflection which confirms the formation of cubic spinel structure without any sign of the secondary phase. After decomposition at  $350^\circ\text{C}$ , the peaks are of typical Ni-Zn ferrites. With increasing sintering temperature, the intensity grows due to better crystallinity. This is due to the penetration process, where crystallites come together and start to grow at favorable conditions (high temperature).<sup>20</sup> During the thermal treatment, the solid-vapor surface of crystals is replaced by a solid-solid interface via diffusion to reduce the overall surface energy which leads to the expansion of volume. Also, at a higher temperature, the nucleation rate is low and the growth rate is high, which gives a high degree of crystallinity. The crystallite size was calculated using the following Scherrer equation and lies in the range of 28–32 nm for all compositions. There is no remarkable trend in crystallite size with increasing  $\text{Ni}^{2+}$  content.

$$D_{311} = \frac{k\lambda}{B \cos \theta} \quad (1)$$

where  $k$  is constant and depends upon the shape of crystallite size = 0.9,  $B$  is the full width at half maximum of intensity for the (311) peak,  $\lambda$  is the wavelength of  $\text{CuK}_\alpha$  radiation ( $1.5406 \text{ \AA}$ ),  $\theta$  is the diffraction angle and  $D$  is the crystallite size.

The experimental ( $a_{\text{exp}}$ ) lattice constant was determined from the Rietveld refinement of the X-ray data and the theoretical ( $a_{\text{th}}$ ) lattice constant was calculated from the following relation and tabulated in Table I.



**Scheme 1** Schematic of an experimental procedure to form the oxalate ferrite complex.

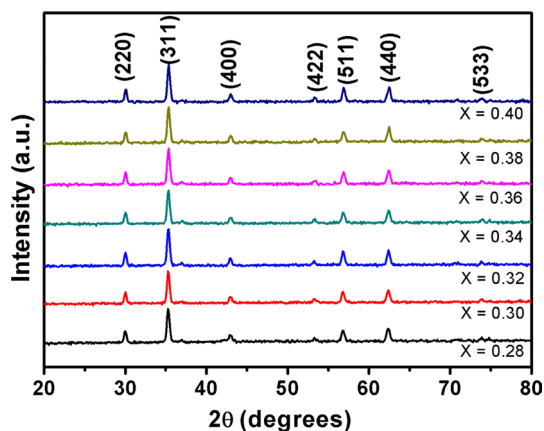


**Fig. 1** XRD pattern of the sintered (1000°C, 4 h)  $\text{Ni}_x\text{Zn}_{1-x}\text{Fe}_2\text{O}_4$  ferrite system.

**Table I** The experimental ( $a_{\text{exp}}$ ) and theoretical ( $a_{\text{th}}$ ) lattice constants of sintered samples.

$X$	$a_{\text{exp}}$	$a_{\text{theo}}$
0.28	8.411	8.387
0.30	8.410	8.383
0.32	8.408	8.378
0.34	8.406	8.375
0.36	8.404	8.372
0.38	8.402	8.367
0.40	8.400	8.364

$$a_{\text{th}} = \frac{8}{3} \sqrt{3} \left[ (r_A + R_o) + \sqrt{3} (r_B + R_o) \right] \quad (2)$$

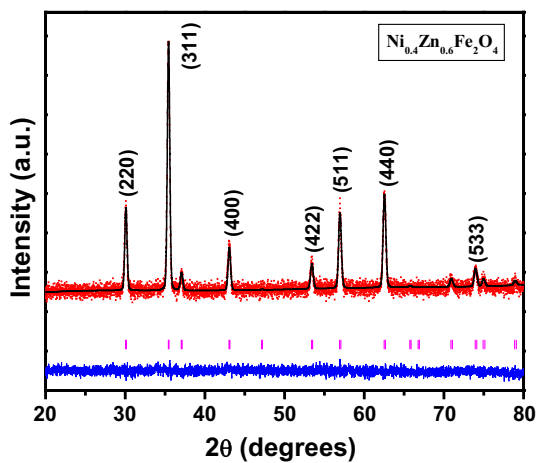
where  $R_o$  is the radius of oxygen ion = 1.38 Å,  $r_A$  and  $r_B$  are ionic radii of tetrahedral [A] and octahedral [B] sites of the spinel lattice, respectively. It is noted that  $a_{\text{exp}}$  and  $a_{\text{th}}$  decrease with increasing  $\text{Ni}^{2+}$  ion content. This decrease in the lattice constant can be attributed to ionic size differences. The difference in  $a_{\text{exp}}$  and  $a_{\text{th}}$  can be attributed to the deviation from the cation distribution and is related to the presence of divalent iron ions  $\text{Fe}^{2+}$  and other crystal imperfections. The present system comprises two kinds of cation distribution, namely, for i)  $\text{NiFe}_2\text{O}_4$  (inverse spinel) and ii)  $\text{ZnFe}_2\text{O}_4$  (normal spinel). As per the spinel-type for the present Ni-Zn mixed ferrite system, there is the possibility of deviation in the cation occupancy at both A and B sites, respectively. Therefore, the difference in  $a_{\text{exp}}$  and  $a_{\text{th}}$  can be attributed to the deviation from the cation distribution of the spinel lattice. Furthermore, the presence of  $\text{Fe}^{2+}$  ions, especially for Ni-Zn ferrite, is very common.

In the case of ferrite, the conduction/hopping mechanism is mainly explained based on the hopping of  $\text{Fe}^{2+}$  and  $\text{Fe}^{3+}$  ions. The present ferrites are sintered at 1000°C, which makes the formation of Zn vacancies possible and thereby increases the presence of  $\text{Fe}^{2+}$  to compensate for the loss of Zn content.<sup>21</sup>

The difference between both  $a_{\text{exp}}$  and  $a_{\text{th}}$  was observed by Kazi et al.<sup>22</sup> for Cu-Zn ferrites and is attributed to the presence of some ferrous ions on octahedral sites with larger radii than  $\text{Fe}^{3+}$ .

**Table II** Parameters obtained from the Rietveld analysis of X-ray diffraction data of  $\text{Ni}_x\text{Zn}_{1-x}\text{Fe}_2\text{O}_4$  samples ( $x = 0.28\text{--}0.40$ ) in space group  $\text{Fd-3m}$  (No. 227). The atoms occupy the positions 8a (1/8,1/8,1/8); 16d (1/2, 1/2, 1/2); and 32e (x,x,x).

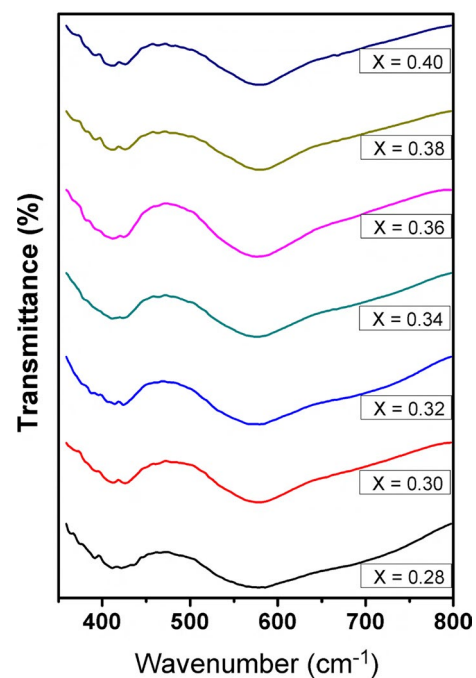
x	0.28	0.30	0.32	0.34	0.36	0.38	0.40
System	$\text{Ni}_{0.28}\text{Zn}_{0.72}\text{Fe}_2\text{O}_4$	$\text{Ni}_{0.30}\text{Zn}_{0.70}\text{Fe}_2\text{O}_4$	$\text{Ni}_{0.32}\text{Zn}_{0.68}\text{Fe}_2\text{O}_4$	$\text{Ni}_{0.34}\text{Zn}_{0.66}\text{Fe}_2\text{O}_4$	$\text{Ni}_{0.36}\text{Zn}_{0.64}\text{Fe}_2\text{O}_4$	$\text{Ni}_{0.38}\text{Zn}_{0.62}\text{Fe}_2\text{O}_4$	$\text{Ni}_{0.40}\text{Zn}_{0.60}\text{Fe}_2\text{O}_4$
A-site (8a)	$\text{Zn}_{0.72}\text{Fe}_{0.28}$	$\text{Zn}_{0.70}\text{Fe}_{0.30}$	$\text{Zn}_{0.68}\text{Fe}_{0.32}$	$\text{Zn}_{0.66}\text{Fe}_{0.34}$	$\text{Zn}_{0.64}\text{Fe}_{0.36}$	$\text{Zn}_{0.62}\text{Fe}_{0.38}$	$\text{Zn}_{0.60}\text{Fe}_{0.40}$
B-site (16d)	$\text{Ni}_{0.28}\text{Fe}_{1.72}$	$\text{Ni}_{0.30}\text{Fe}_{1.70}$	$\text{Ni}_{0.32}\text{Fe}_{1.68}$	$\text{Ni}_{0.34}\text{Fe}_{1.66}$	$\text{Ni}_{0.36}\text{Fe}_{1.64}$	$\text{Ni}_{0.38}\text{Fe}_{1.62}$	$\text{Ni}_{0.40}\text{Fe}_{1.60}$
O (x)	0.2575(5)	0.2579(5)	0.2586(4)	0.2590(4)	0.2581(4)	0.2566(4)	0.2581(4)
a (Å)	8.4112(5)	8.4102(5)	8.4084(5)	8.4066(4)	8.4040(4)	8.4022(4)	8.400(4)
V (Å <sup>3</sup> )	595.07(5)	594.86(5)	594.48(5)	594.11(4)	593.557(5)	593.18(5)	592.92(5)

**Fig. 2** Rietveld refined X-ray diffraction pattern of  $\text{Ni}_{0.4}\text{Zn}_{0.6}\text{Fe}_2\text{O}_4$ .

The following Table II describes the parameters obtained from Rietveld refinement of all developed ferrite systems to get exact contribution of doped atoms in the system. In this refinement, the cell parameter, position of oxygen atoms, and occupancy was varied. Figure 2 shows a refined X-ray diffraction pattern of  $\text{Ni}_{0.4}\text{Zn}_{0.6}\text{Fe}_2\text{O}_4$ , typical for the entire series of samples. The continuous line through the observed data points ( $I_{\text{obs}}$ ) indicates the calculated intensity ( $I_{\text{calc}}$ ). The tick marks indicate the Bragg positions and the continuous line in blue indicates the difference curve ( $I_{\text{obs}} - I_{\text{calc}}$ ). The value of cell parameter obtained for sample  $x = 0.28$  is in close agreement with that reported<sup>23</sup>

### Fourier Transform Infrared Spectroscopic Analysis

In combination with X-ray diffraction patterns, Fourier transform infrared spectroscopy (FTIR) was used to analyze the matrix composition of the developed ferrite. Figure 3 shows the FTIR spectra of the developed  $\text{Ni}_x\text{Zn}_{1-x}\text{Fe}_2\text{O}_4$  system. Two absorption bands corresponding to the vibration of tetrahedral and octahedral complexes at  $580\text{ cm}^{-1}$  and  $411\text{ cm}^{-1}$  were observed, displaying the formation of spinel

**Fig. 3** FTIR spectra of  $\text{Ni}_x\text{Zn}_{1-x}\text{Fe}_2\text{O}_4$  ferrite system.

ferrite structure. This confirms the XRD analysis, where the materials show all the characteristic reflections of cubic spinel ferrites. The absorption band  $\nu_1$  was caused by stretching of tetrahedral metal ion and oxygen bonding, whereas  $\nu_2$  was caused by the vibration of oxygen in the direction perpendicular to the axis joining tetrahedral ion and oxygen ion. Waldron<sup>24</sup> attributed the absorption band  $\nu_1$  to the intrinsic vibration of tetrahedral groups corresponding to the highest restoring force and band  $\nu_2$  to octahedral groups which are due to bond bending vibrations.

The difference in the position of two bands  $\nu_1$  and  $\nu_2$  could be related to the difference in  $\text{Fe}^{3+}$  and  $\text{O}^{2-}$  distance for the A site and the B site. In general, the distance of the Fe-O bond at the A site is 0.189 nm, whereas, for the B site, it is 0.199 nm.<sup>25</sup> In the present study, the absorption bands of the developed Ni-Zn ferrite system were found in the

forementioned range. The force constants corresponding to the tetrahedral and octahedral complexes are calculated by using the following formulae<sup>26</sup> and the results are tabulated in Table III.

$$K_t = 7.62 \times M_1 \times \vartheta_1^2 \times 10^{-7} \tag{3}$$

$$K_o = 10.62 \times \frac{M_2}{2} \times \vartheta_2^2 \times 10^{-7} \tag{4}$$

where  $K_0$  = force constant of the octahedral site,  $K_t$  = force constant of the tetrahedral site,  $M_1$  = molecular weight of the tetrahedral site,  $M_2$  = molecular weight of the octahedral site,  $\nu_1$  = corresponding center frequency on the tetrahedral site,  $\nu_2$  = corresponding center frequency on the octahedral site.

### Elastic Properties

The elastic moduli which are frequently employed in engineering practice include Young’s modulus, shear modulus, bulk modulus, and Poisson’s ratio. In industry, elastic data are used to determine the strength of materials. When considering an application of any polycrystalline material (spinel ferrite in the present case) subjected to mechanical stresses, knowledge of its magnetic, electric/dielectric response and elastic properties aids in determining the material’s suitability for the specific applications viz. high-speed digital tapes, operating devices, magnetic drug delivery, magnetic fluid, and high-density information storage.<sup>27–29</sup> Knowledge of elastic constants elucidates the nature of

interatomic and interionic forces in solids from the standpoint of fundamental study. In all total, there are 36 elastic moduli available for the rheological studies of any material. However, in the case of isotropic and homogeneous materials such as spinel ferrites, the number reduces to barely 3. The obtained values of these elastic moduli are listed in Table III, which are calculated using the following formulae.

$$L = \frac{K}{a} \tag{5}$$

$$G = \rho_x \times (V_T)^2 \tag{6}$$

$$B = L - \left(\frac{4}{3}\right)G \tag{7}$$

$$E = (1 + \sigma)2G \tag{8}$$

It is observed that the magnitude of elastic moduli is almost constant with increasing Ni<sup>2+</sup> content in the present ferrite system. The elastic moduli can be greatly influenced by the presence of porosity, a second phase, and impurities. The porosity is a dominating factor in determining the elastic moduli, as it determines the overall strength of the synthesized material. An increase in porosity leads to a decrease in the density of the material. These, in turn, vary the magnitude of elastic moduli and vice versa. In the present case, the density of the synthesized material is very high (revealed in x-ray density) and the pore fraction is minimum (SEM) (See Table IV). Therefore, the elastic moduli of the present ferrites show fairly constant values with increasing Ni<sup>2+</sup> content.

**Table III** Data on vibrational bands ( $\nu_1$  and  $\nu_2$ ), force constants ( $K_t$  and  $K_0$ ) and longitudinal modulus ( $L$ ), shear modulus ( $G$ ), Bulk modulus ( $B$ ), Young’s modulus ( $E$ ) for the present ferrite system

X	$\nu_1$	$\nu_2$	$K_t$	$K_0$	L	G	B	E
0.28	575.56	412.72	158.3	101.74	154.897	51.6325	86.0541	129.0812
0.30	576.1	412.43	158.11	101.65	154.806	51.6022	86.0036	129.0054
0.32	577.73	412.24	158.52	101.61	155.119	51.7062	86.177	129.2655
0.34	578.5	411.9	158.33	101.49	154.991	51.6636	86.1061	129.1591
0.36	578.99	411.52	158.24	101.36	154.911	51.637	86.0617	129.0925
0.38	579.13	411.47	157.83	101.38	154.774	51.5914	85.9856	128.9784
0.40	581.31	411.27	158.53	101.34	155.219	51.7397	86.2328	129.3491

**Table IV** Data on longitudinal wave velocity ( $V_L$ ) and transverse wave velocity ( $V_T$ ), mean wave velocity ( $V_m$ ), Poisson’s ratio ( $\sigma$ ), X-ray density ( $\rho_x$ ) and actual density ( $\rho_a$ ) and pore fraction ( $p$ )

X	$V_L$	$V_T$	$\sigma$	$\rho_x$	$\rho_a$	p
0.28	5407.8	3122.7	0.2505	5.3729	5.2994	0.0136
0.30	5538.3	3197.6	0.2499	5.3761	5.0796	0.0551
0.32	5557.2	3208.5	0.2499	5.3838	5.0294	0.0658
0.34	5439.1	3140.3	0.2500	5.3862	5.1999	0.0346
0.36	5443.2	3142.7	0.2499	5.3886	5.1995	0.0351
0.38	5493.1	3171.5	0.2499	5.3949	5.1796	0.0380
0.40	5495.7	3173.0	0.2499	5.3988	5.1197	0.0517



### Microstructural and Elemental Analysis

Figure 4 illustrates the SEM images of selected compositions with different magnifications, which displayed the formation of small particles. Unlike the combustion route of ferrite synthesis, the formation of small and homogeneous particles is possible using an oxalate precursor. The aggregation is considerably limited, due to the dropwise addition of precursors moieties in the reaction solvent and thereby formation of ferrite material molecule-by-molecule. The magnified images of sample  $x = 0.32$  are in the fitness of an argument made above.

From the obtained micrographs, average grain size ( $D_{av}$ ) has been calculated using the following formula<sup>30</sup>:

$$D_{av} = \frac{1.5L}{MN} \quad (9)$$

where  $L$  is the total test line length;  $M$  is the magnification;  $N$  is the total number of intercepts.

From Table V, it is clear that the average grain size lies between 0.9 to 1.2  $\mu\text{m}$  for all the ferrite samples sintered at 1050°C. It is also evident that the grains were not separated by a large margin, suggesting that the intra-granular porosity is minimal. Further, the grain size does not show any particular trend with increasing  $\text{Ni}^{2+}$  content.

**Table V** Average grain size values of the ferrites with  $x = 0.28, 0.32,$  and  $0.36$ .

$X$	average grain size, $D_{av}$ ( $\mu\text{m}$ )
0.28	0.9
0.32	1.2
0.36	1.0

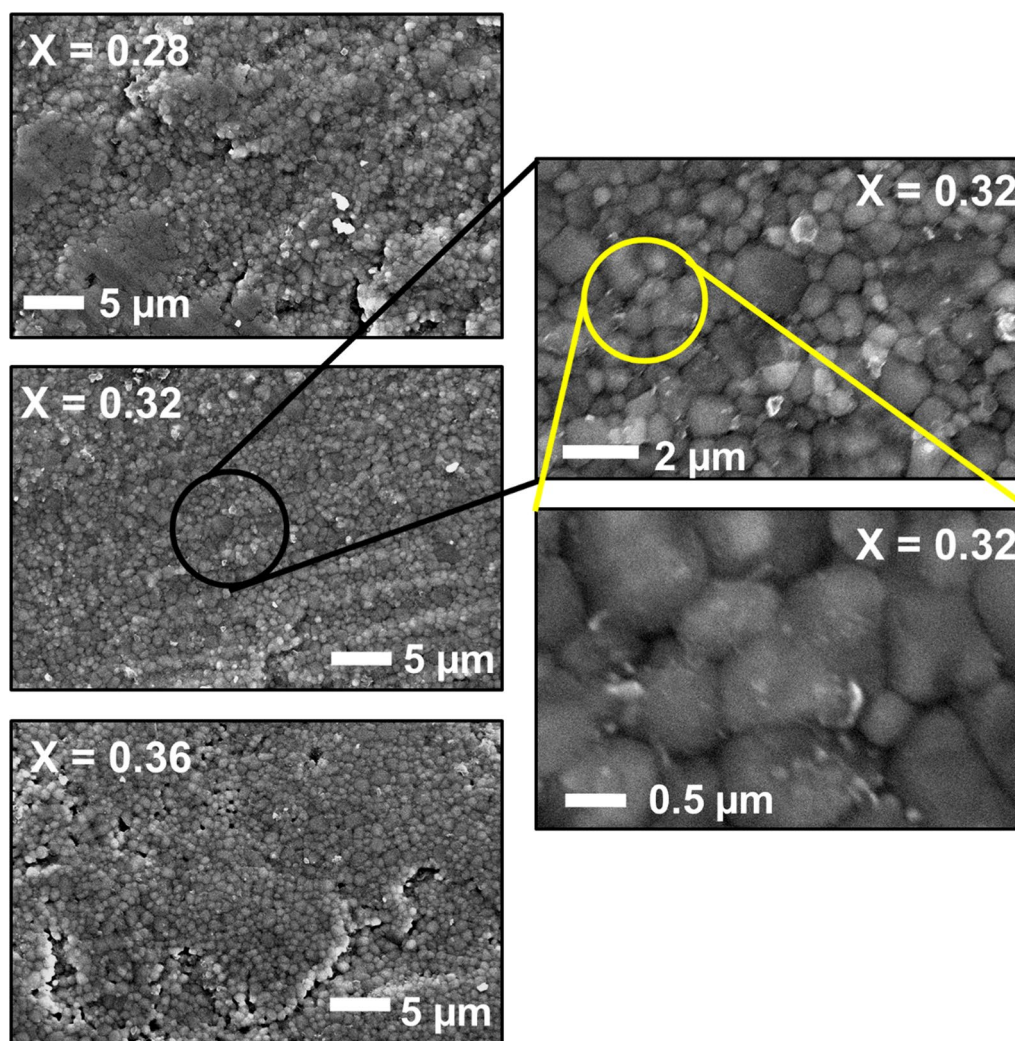


**Fig. 4** SEM images of  $\text{Ni}_x\text{Zn}_{1-x}\text{Fe}_2\text{O}_4$  ferrite system, with  $x = 0.28, 0.32,$  and  $0.36$ .

**Fig. 5** EDAX spectra of developed ferrites with  $x = 0.28$ , 0.32, 0.36 and 0.40.

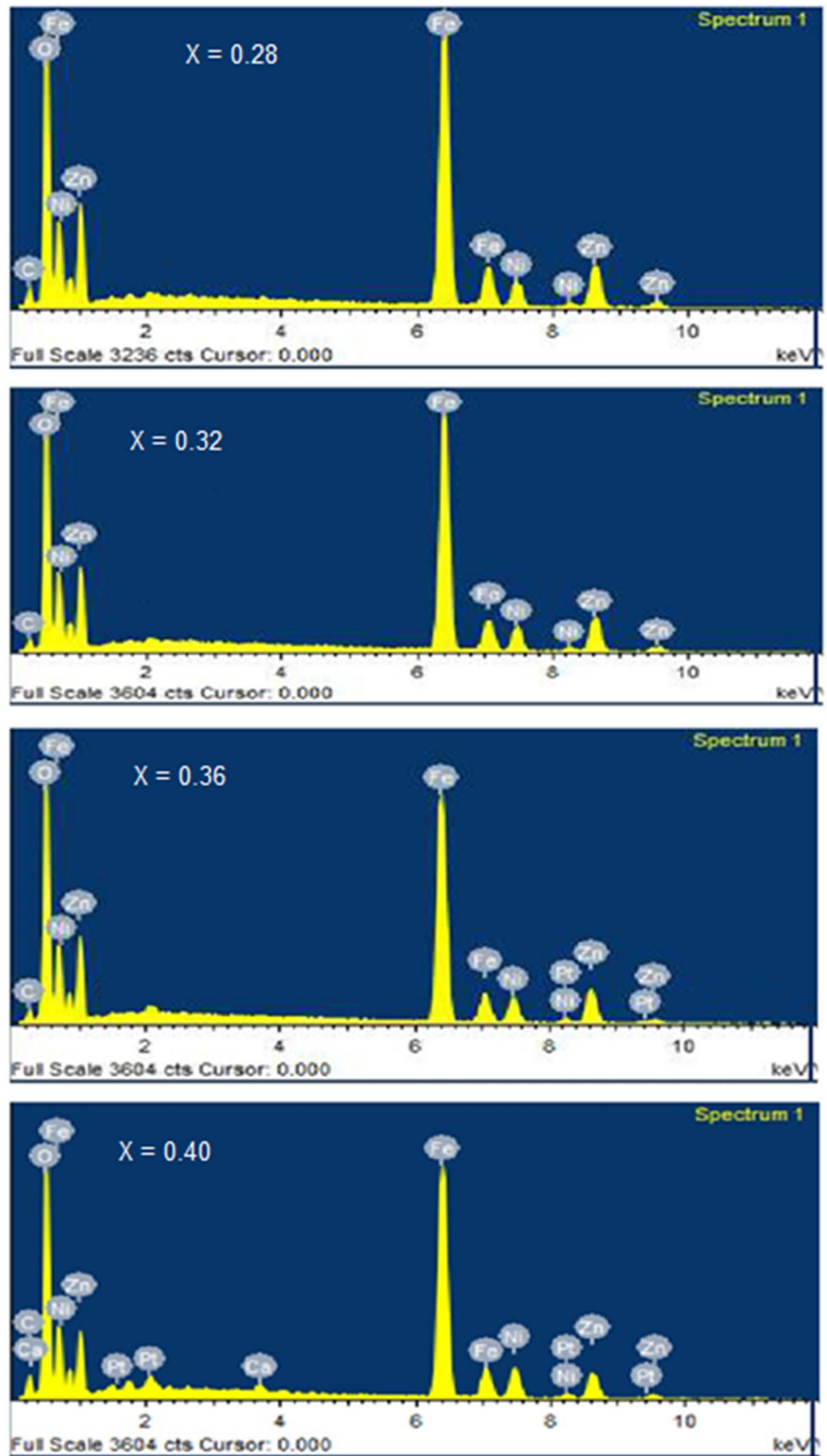


Figure 5 illustrates the EDAX spectra of selected compositions ( $x = 0.28, 0.32, 0.36$  and  $0.40$ ). The elemental composition that resulted from EDAX analysis shows the presence of Ni, Zn, Fe and O according to atomic ratios taken in the initial precursors for respective samples. Apart from the native/constituent elements, other minor peaks are also observed in some compositions which might be due to impurities in the starting materials. Similar observations of the C substrate peak and other minor peaks are also observed in the case of  $\text{MnFe}_2\text{O}_4$  ferrite by Zipare et al. <sup>31</sup>

## Conclusions

A robust synthesis approach for complex spinel ferrite materials using oxalate precursor chemistry is discussed. Simple metal acetates and oxalate precursor in aqueous solution are used to develop the nanocrystalline  $\text{Ni}_x\text{Zn}_{1-x}\text{Fe}_2\text{O}_4$  ( $x = 0.28, 0.30, 0.32, 0.34, 0.36, 0.38, 0.40$ ) ferrites. Initially,  $\text{Fe}^{2+}$  acetate is prepared to precipitate ferrite using oxalate chemistry. XRD analysis of calcined ( $350^\circ\text{C}$ , 3 h) and sintered ( $1000^\circ\text{C}$ , 10 h)  $\text{Ni}_x\text{Zn}_{1-x}\text{Fe}_2\text{O}_4$  ferrite displayed all the characteristic reflections of cubic spinel ferrites with most intense (311) reflection, without any sign of a secondary phase. It was observed that both experimental and theoretical lattice parameter values were found to decrease with increasing the  $\text{Ni}^{2+}$  ion content. FTIR spectra designate two main absorption bands, one for the tetrahedral site around  $575$  to  $580\text{ cm}^{-1}$  and the other for the octahedral site around  $411$  to  $413\text{ cm}^{-1}$ . The force constants  $K_t$  and  $K_o$  for the two sites were calculated with an increase in  $\text{Ni}^{2+}$  content. The magnitude of elastic moduli is found to be independent (fairly constant) with increasing  $\text{Ni}^{2+}$  content. The morphological analysis (SEM) showed the formation of small and homogeneous particles, which is possible using an oxalate precursor. The elemental analysis confirmed the presence of Ni, Zn, Fe and O with respect to their stoichiometric amount. The present study widens the research spread of synthesizing complex spinel ferrites.

**Supplementary Information** The online version contains supplementary material available at <https://doi.org/10.1007/s11664-022-09582-y>.

**Conflict of interest** The authors declare no competing interests.

## References

1. Y. Cheng, J. Tian, J. Lin, S. Wang, S. Xie, Y. Pei, S. Yan, M. Qiao, H. Xu, and B. Zong, Potassium-promoted magnesium ferrite on 3D porous graphene as highly efficient catalyst for CO hydrogenation to lower olefins. *J. Catal.* 374, 24 (2019).
2. P.J. Jessy, V. Bambole, R.R. Deshmukh, and N. Patel, Reduced power consumption in nickel zinc ferrite nanoparticles doped blue phase chiral nematic liquid crystal devices. *J. Mol. Liq.* 281, 480 (2019).
3. S.Y. Srinivasan, K.M. Paknikar, D. Bodas, and V. Gajbhiye, Applications of cobalt ferrite nanoparticles in biomedical nanotechnology. *Nanomedicine* 13, 10 (2018).
4. S. Chakma, G. K. Dinesh, S. Chakraborty, and V. S. Moholkar, Investigation in Sono-photocatalysis Process Using Doped Catalyst and Ferrite Nanoparticles for Wastewater Treatment, in ed. by A.A. Inamuddin, E. Lichtfouse, *Nanophotocatalysis and Environmental Applications. Environmental Chemistry for a Sustainable World*, vol 30 (Springer, 2020), p. 171-194.
5. M. Tahir Farid, I. Ahmad, M. Kanwal, G. Murtaza, M. Hussain, S.A. Khan, and I. Ali, Synthesis, electrical and magnetic properties of Pr-substituted Mn ferrites for high-frequency applications. *J. Electron. Mater.* 46, 1826 (2017).
6. M. N. Akhtar, M. A. Khan, M. Ahmad, M.S. Nazir, M. Imran, A. Ali, A. Sattar, and G. Murtaza, Evaluation of structural, morphological and magnetic properties of  $\text{CuZnNi}$  ( $\text{Cu}_x\text{Zn}_{0.5-x}\text{Ni}_{0.5}\text{Fe}_2\text{O}_4$ ) nanocrystalline ferrites for core, switching and MLCI's applications. *J. Magn. Magn. Mater.* 421 (1), 260 (2017)
7. S.P. Dalawai, T.J. Shinde, A.B. Gadkari, and P.N. Vasambekar, Influence of  $\text{Ni}^{2+}$  and  $\text{Sn}^{4+}$  substitution on gas sensing behaviour of zinc ferrite thick films. *J. Solid State Electrochem* 20, 2363 (2016).
8. N. Ikramullah, F. Ali, Z. Sheikh, M. Bilal, and I. Ahmad, Photocatalytic performance of zinc ferrite magnetic nanostructures for efficient eriochrome black-T degradation from the aqueous environment under unfiltered sunlight. *Water Air Soil Pollut.* 231, 59 (2020).
9. P. Gao, X. Hua, V. Degirmenci, D. Rooney, M. Khraisheh, R. Pollard, R. Bouiman, and E.V. Rebrav, Structural and magnetic properties of  $\text{Ni}_x\text{Zn}_{1-x}\text{Fe}_2\text{O}_4$  ( $x = 0, 0.5, 1$ ) nanopowder prepared by sol-gel method. *J. Magn. Magn. Mater.* 348, 44 (2013).
10. B.S. Badireddi, and V. Raghavendra, XRD, TEM, Magnetic studies on  $\text{Ni}_x\text{Zn}_{1-x}\text{Fe}_2\text{O}_4$  (Where  $x = 0.2, 0.4, 0.5, 0.6$  and  $0.8$ ) nano scale particles by chemical co-precipitation method. *Int. Let. Chem. Phys. Astron.* 60, 20 (2015).
11. D.H. Chen and X. Hea, Synthesis of nickel ferrite nanoparticles by sol-gel method. *Mater. Res. Bull.* 36, 1369 (2001).
12. K. Sue, M. Aoki, T. Sato, D. Nishio-Hamane, S. Kawasaki, Y. Hakuta, Y. Takebayashi, S. Yoda, T. Furuya, T. Sato, and T. Hiaki, Continuous hydrothermal synthesis of nickel ferrite nanoparticles using a central collision-type micromixer: effects of temperature, residence time, metal salt molality, and NaOH addition on conversion, particle size, and crystal phase. *Ind. Eng. Chem. Res.* 50, 9625 (2011).
13. L. Hao, Y. Zhao, Q. Jiao, and P. Chen, Synthesis of zinc-nickel ferrite nanorods and their magnetic properties. *RSC Adv.* 4, 15650 (2014).
14. A. Verma and R. Chatterjee, Effect of zinc substitution on structural, electrical and magnetic properties of mixed Mn-Zn and Ni-Zn ferrites synthesized by citrate precursor techniques. *J. Magn. Magn. Mater.* 306, 313 (2006).
15. S. Kumar, V. Singh, S. Aggrawal, U. Mandal, and R.K. Kotnala, Synthesis of nanocrystalline  $\text{Ni}_{0.5}\text{Zn}_{0.5}\text{Fe}_2\text{O}_4$  ferrite and study of its magnetic behavior at different temperature. *Mater. Sci. Eng. (B)* 166, 76 (2010).
16. Y. Koseoglu, Structural and magnetic properties of Cr doped Ni-Zn ferrite nano particles prepared by surfactant assisted hydrothermal technique. *Ceram. Inter.* 41, 6417 (2015).
17. A.S. Dzunuzovic, N.I. Illice, M.M. Vijatovic Petrovic, J.D. Bobic, B. Stojadinovic, Z. Dohcevic Mitrovic, and B.D. Stojanovic,



- Structure and properties of Ni-Zn ferrites obtained by auto combustion method. *J. Magn. Mater.* **374**, 245 (2015)
18. V.D. Sudheesh, J. Nehra, A. Vinesh, V. Sebastian, N. Lukshmi, D.P. Dutta, V.R. Reddy, K. Venugopalan, and A. Gupta, Investigations of structural and magnetic properties of  $\text{Ni}_{0.5}\text{Zn}_{0.5}\text{Fe}_2\text{O}_4$  nano powders prepared by self combustion method. *Mat. Res. Bull.* **48**, 698 (2013).
  19. K. Velmurugan, V.S.K. Venkatachalapathy, and S. Sendhilnathan, Thermogravimetric and magnetic properties of  $\text{Ni}_{1-x}\text{Zn}_x\text{Fe}_2\text{O}_4$  nanoparticles synthesized by coprecipitation. *J. Mater. Res.* **12**, 529 (2009).
  20. L. Rezlescu, E. Rezlescu, P.D. Popa, and N. Rezlescu, Fine barium hexaferrite powder prepared by crystallization of glass. *J. Magn. Mater.* **193**, 288–290 (1999).
  21. J. Massoudi, M. Smari, K. Nouri, E. Dhahri, K. Khirouni, S. Bertaina, L. Bessaïc, and E.K. Hlilf, Magnetic and spectroscopic properties of Ni-Zn-Al ferrite spinel: from the nanoscale to micro-scale. *RSC Adv.* **10**, 34556 (2020).
  22. K.H. Maria, S. Choudhary, and M.A. Hakim, Structural transformation and hysteresis behavior of Cu-Zn ferrites. *Int. Nano Lett.* **3**, 1 (2013).
  23. A.R. Das, V.S. Ananthan, and D.C. Khan, Lattice parameter variation and magnetization studies on titanium-, zirconium-, and tin-substituted nickel-zinc ferrites. *J. Appl. Phys.* **57**, 4189 (1985).
  24. R.D. Waldron, Infrared spectra of ferrites. *Phys. Rev. Lett.* **99**, 1727 (1955).
  25. S. Dabagh, K. Chaudhary, Z. Haider, and J. Ali, Study of structural phase transformation and hysteresis behavior of inverse-spinel  $\alpha$ -ferrite nanoparticles synthesized by co-precipitation method. *Res. Phys.* **8**, 93 (2018).
  26. T.K. Pathak, J.J.U. Buch, U.N. Trivedi, H.H. Joshi, and K.B. Modi, Infrared spectroscopy and elastic properties of nanocrystalline Mg-Mn ferrites prepared by co-precipitation technique. *J. Nanosci. Nanotechnol.* **8**, 4181 (2008).
  27. A. Goldman, Understanding ferrites. *ACS. Bulletin* **63**, 582 (1984).
  28. P. Ravindranathan and K.C. Patil, Novel solid solution precursor method for the preparation of ultrafine Ni-Zn ferrites. *J. Mat. Sci.* **22**, 3261 (1987).
  29. H. Igarash, and K. Okazaki, Effects of porosity and grain size on the magnetic properties of NiZn ferrite. *J. Am. Ceram. Soc* **60**, 54 (1977).
  30. M.P. Reddy, W. Madhuri, N.R. Reddy, K.V. Siva Kumar, V.R.K. Murthy, and R.R. Reddy, Magnetic properties of Ni-Zn ferrites prepared by microwave sintering method. *J. Electroceram.* **28**, 1–9 (2012).
  31. K. Zipare, J. Dhumal, S. Bandgar, V. Mathe, and G. Shahane, Superparamagnetic manganese ferrite nanoparticle: synthesis and magnetic properties. *J. Nanosci. Nanotechnol.* **1**, 178 (2015).

**Publisher's Note** Springer Nature remains neutral with regard to jurisdictional claims in published maps and institutional affiliations.